




Facile synthesis of Fe₃O₄/NiFe₂O₄ nanosheets with enhanced Lithium-ion storage by one-step chemical dealloying

Hang Xu¹, Xinlu Wang^{1,*} , Huan Liu¹, Jinxian Wang^{1,*}, Xiangting Dong¹, Guixia Liu¹, Wensheng Yu¹, Ying Yang¹, and Hongbo Zhang¹

¹Key Laboratory of Applied Chemistry and Nanotechnology at Universities of Jilin Province, Department of Chemistry and Environmental Engineering, Changchun University of Science and Technology, Changchun 130022, Jilin, People's Republic of China

Received: 1 June 2018

Accepted: 20 July 2018

Published online:

26 July 2018

© Springer Science+Business Media, LLC, part of Springer Nature 2018

ABSTRACT

Fe₃O₄/NiFe₂O₄ nanosheets as anode materials for lithium-ion batteries have been successfully prepared by a facile one-step dealloying method of Al–Fe–Ni alloy precursor. Herein, the XRD results and XPS spectra indicated that the product consists of cubic NiFe₂O₄ and Fe₃O₄. Scanning electronic microscopy and transmission electron microscopy images showed the homogenous distribution of Fe₃O₄/NiFe₂O₄ in the quasi-hexagonal nanosheets rather than irregular clusters. Besides nanostructures, their electrochemical performances were also enhanced due to the doping of nickel when comparing with the Fe₃O₄ obtained by dealloying Al–Fe precursor. Cycling and rate tests elicited the DAFN has the Fe₃O₄/NiFe₂O₄ product exhibit a higher initial capacity of ~ 1437 mAh g⁻¹ at 200 mA g⁻¹ and modified rate performances, especially they hold a doubled reversible capacity over 500 mAh g⁻¹ after 750 times cycling at 200 mA g⁻¹. Cyclic voltammetry, charge–discharge tests and electrochemical impedance spectra measurements further demonstrated the reinforced initial capacity and cycling stability of the DAFN could be associated with the shortened diffusion pathways and synergistic effect of Fe₃O₄ and NiFe₂O₄. The facile and low-cost processing method accompanied with the well-performed product exhibit a promising prospect in the application of lithium-ion storage.

Introduction

Compared with conventional forms of power supplies, rechargeable Li-ion batteries (LIBs) have been more widely employed in communication, electric

vehicles and other most advanced fields due to their sustainable high capacity, energy density, cycling stability and peerless portability [1–3]. With a low theoretical capacity of 372 mAh g⁻¹, conventional graphite has occupied the majority component of the

Address correspondence to E-mail: xinluwang@163.com; wjx87@sina.com

anode materials in commercial LIBs for decades, which can hardly meet the ever-growing demands for high power sources [4]. In terms of exploring candidates for replacement, profuse efforts have made to reinforce the performance by numerous attempts [5].

Among a variety of modification, introducing metal oxides [4, 6], especially inorganic transition metal oxides (TMOs) as anode materials have triggered intensive attention owing to high theoretical capacity and long lifespan compared with graphite [7–10]. It is noteworthy that iron oxides are of great advantage such as natural abundance, eco-compatibility and low price [11, 12] so that they have strongly attracted much attention for further research and mass production [13]. However, the limits of iron oxides inherent on poor lithiation activity, low electrical conductivity, large volume change and severe agglomeration [14–17] during the conversion reaction have severely impeded the practical application, especially the strong impact on rate performance and capacity retention [14, 18]. To address these shortcomings, a series of attempts to enhance the electrical conductivity, shorten the Li^+ diffusion distances, alleviate the pulverization and agglomeration have utilized [14, 19–24]. Several effective methods have pointed out that the nanostructured binary transition oxides have the synergistic effects through reinforcing or modifying each other to generate the enhanced electrochemical activity [25–28]. Inspired by our previous work [9] and references reported [22, 29], we noticed that the nickel-incorporated nanostructured oxides can contribute to the better lithium activity and storage capability [26, 30]. Thus, we intended to obtain a Fe-based oxide material with Ni-incorporated versus unsophisticated Fe-based oxides. Hoping that the product could combine the advantages of nanostructured Ni and Fe metal oxides with superior performances as anode material by our rationally designed preparation processes.

In view of considerable incorporation methods including hydrothermal [7, 29, 31, 32], co-precipitation [11], physical/chemical deposition [33, 34], and mechanical-milling [14, 35] were carried out with disadvantages such as complex controlling conditions, high synthesis costs and low output unsolved. Herein, to tackle this problem, we introduced a novel one-step chemical dealloying method that can be interpreted as a reaction–diffusion process, where the less noble metal in alloy is selectively dissolved into

an acid or alkaline solution at the solid/liquid interface, thus generating a porous structure accompanied with the spontaneous oxidation and regroup of the remaining parts [36, 37]. This facile and straightforward approach is easy to realize the controllable component and uniform distribution in the product which has proved to be efficient in our previous works [9, 37, 38]. In addition, the versatile and practical method has successfully used in many applied fields such as gas sensors [39], catalysts [40], and structural materials [41] for years.

Inspired by the aforementioned statement, our focus is to explore high-performance anode by introducing Ni oxide as well as tailoring the nanostructure. Bearing this in mind, our work selected and compared Al–Fe–Ni (AFN) ternary alloy and Al–Fe (AF) binary alloy as precursors under the same dealloying process in NaOH solution. Results showed during the removal of Al, neither the remained Ni nor Fe formed metallic phase but oxidized and self-assembled to a certain morphology eventually. Particularly, the as-made AFN sample showed quasi-hexagonal nanosheets with interconnected voids which can effectively accommodates volume change and decrease the diffusion distance during conversion processes. Electrochemical examinations also confirmed that it possesses enhanced capacity, rate performance, fast ion diffusion and electronic transfer. Taken advantage of simple preparation and excellent electrochemical performance mentioned above, the as-made $\text{Fe}_3\text{O}_4/\text{NiFe}_2\text{O}_4$ nanocomposite showed promising application as anode material for LIBs. Also, considering that neither environmental hazards participated nor produced, the dealloying method could be competent to our following researches and upcoming industrial manufacture.

Experimental section

Sample preparation

The Al–Fe–Ni ($\text{Al}_{86}\text{Fe}_{12}\text{Ni}_2$ namely, marked as AFN) ternary alloy ingots were obtained by refining high purity (99.9%) of Al, Fe and Ni in arc-furnace, while the $\text{Al}_{86}\text{Fe}_{14}$ (AF) binary alloy refinement were almost coincident except for Ni element's absence. Later on, we adapted a melt-spinning procedure under the argon atmosphere and obtained numerous alloy

ribbons as dealloying precursors with the thickness around 50 μm . Next, the precursors underwent a selective etching by 2 M NaOH solution under the air condition at room temperature for 48 h to ensure no obvious bubbles emerged. The resultant were washed three times with ultra-pure water (18.2 M Ω cm) and ethanol by turns then preserved in a drying box at 60 °C overnight to have the dealloyed AFN and AF products (DAFN and DAF, respectively) obtained eventually.

Material characterization

The crystal structure of the products were further analyzed by a powder X-ray diffractometer (XRD, Tongda TD-3000) using Cu K α radiation at the scan rate of 0.02° s⁻¹ with 2-theta degrees ranges from 10° to 90°. The microstructure and chemical composition of the specimens were observed through field emission scanning electron microscopy (SEM, JEOL JSM-7610F) equipped with an X-sight energy-dispersive X-ray spectrometer (EDS, Oxford, X-Max). Low-magnification and high-resolution transmission electron microscopy (TEM and HRTEM) images were captured at the working voltage of 20 kV by using JEM-2100. Surface structural properties analysis of the as-made products were performed on an X-ray photoelectron spectroscopy (XPS, ESCALab 250), using monochromatized Mg K α X-ray as the excitation source, choosing C 1s (284.6 eV) as the reference line.

Electrochemical tests

The electrochemical behavior was evaluated by assembling coin-type cell (size: CR2032) in an argon-filled humidity-free glove box with lithium foils as the counter and reference electrodes versus the dealloyed products as the working electrodes. To prepare the working electrodes, the active material (AF and AFN, respectively), acetylene black, polyvinylidene difluoride (PVDF) were mixed at a weight ratio of 8:1:1 in N-methyl-2-pyrrolidone (NMP). After the mixed slurry was milled uniformly, it was blade coated onto a Cu foil and dried under vacuum at 80 °C for 12 h. The mass loading of each product on the electrode was weighted about 1.0–1.2 mg per unit area. The working electrode and lithium foil electrode were electronically separated by a Celgard 2320 microporous membrane and immersed in the electrolyte composed of 1 M LiPF₆

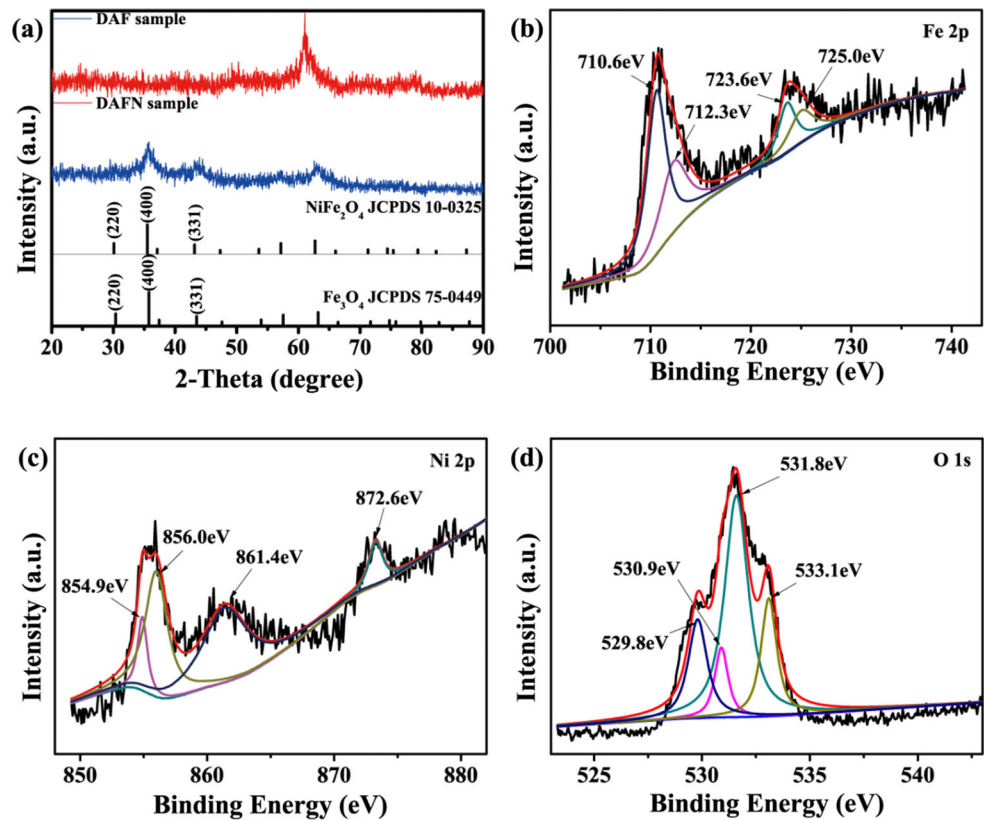
dissolved in dimethyl carbonate (DMC) –ethylene carbonate (EC) mixture at the volume ratio of 1:1. For electrochemical test, the charge/discharge performances, Columbic efficiencies, cycling and rate capacities were carried out galvanostatically between 0.01 and 3.0 V in a NEWARE BTS 5 V–10 mA computer-controlled testers (Shenzhen, China) with various current densities. Cyclic voltammetry (CV) test at the scan rate of 0.1 mV s⁻¹ and the electrochemical impedance spectroscopy (EIS) measurement over the frequency range between 0.01 Hz and 100 kHz were carried out through an electrochemical workstation (CHI-760D, Shanghai, China).

Results and discussion

The phase information of different samples was characterized by XRD measurement to ascertain the crystalline structure. It could be observed from the XRD patterns in Figure S1 that the AF and AFN alloy ribbons can be well assigned to cubic Al (JCPDS No. 04-0787) and monoclinic Al_{76.8}Fe₂₄ (JCPDS No. 38-1147), while the AFN alloy has the extra component of cubic kamacite (Fe, Ni JCPDS No. 04-0787) detected. In the meantime, as is conveyed from the two broaden peaks in Fig. 1a, the dealloyed product DAF and DAFN possess cubic Fe₃O₄ (JCPDS No. 75-0449) phase at the first identification, which is a convincing proof of the total removal of metallic Al. To facilitate our recognition, a heat treatment was carried out through annealing at 600 °C for 2 h in Ar protected atmosphere. As shown in Figure S2, it could be expounded that besides cubic Fe₃O₄ (JCPDS No. 75-0449), the DAFN product has the cubic NiFe₂O₄ (JCPDS No. 10-0325) well indexed. When comparing with the calculated lattice parameters in Table S1, it is noteworthy that the interplanar spacing of the DAFN (8.336 Å) is larger than the DAF (8.321 Å) and Fe₃O₄ (8.320 Å), smaller than but closer to NiFe₂O₄ (8.339 Å). Thus, we can conclude that the incorporation of Ni could enlarge the lattice space of the dealloyed product. As described above, we deduced that the main constitute of the DAF and DAFN are nearly the same but for DAFN contains additional Nickel ferrite.

In the two samples, the valence state of each element was checked out by XPS analyzing the surface of the dealloyed products. As acquainted in Fig. 1b and Figure S3(b), both of the DAFN and DAF

Figure 1 a XRD patterns of the DAF and DAFN products etched by 2 M NaOH for 48 h in air. XPS survey of the as-dealloyed DAFN sample: b Fe 2p, c Ni 2p and d O 1s, respectively.

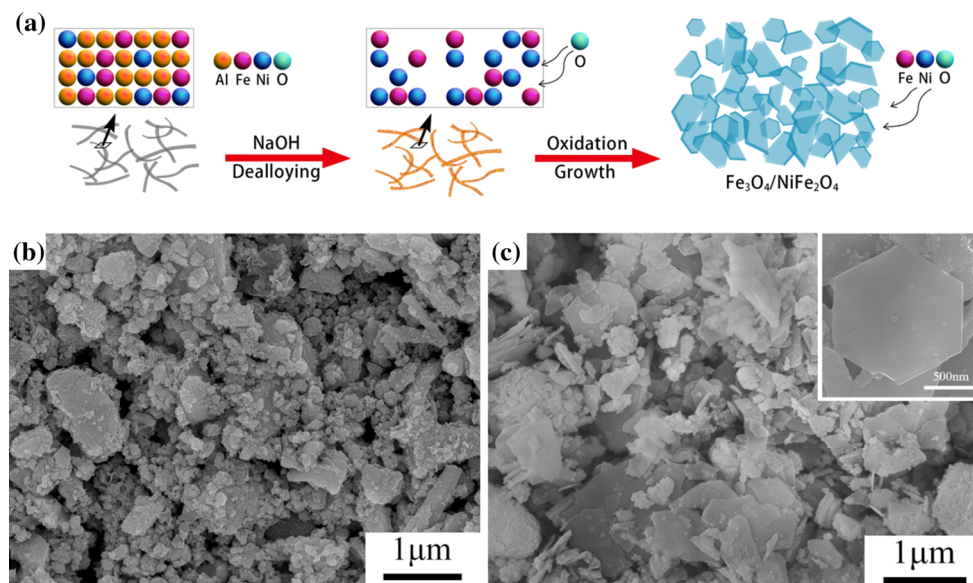


samples possess the Fe $2p_{3/2}$ and Fe $2p_{1/2}$ peaks of the Fe_3O_4 at 712.3 [42] and 723.6 eV [43]. In the meantime, the DAFN sample has the additional Fe $2p_{3/2}$ peaks addressed at 710.6 eV [44] and the Fe $2p_{1/2}$ peaks at 725.0 eV [45] which is belonged to NiFe_2O_4 . The DAF has the Fe $2p_{3/2}$ characteristic peaks of Fe_3O_4 at 710.2 [42] and 711.0 eV [43]. It can also be observed from Fig. 1d and Figure S3(c) that the O 1s peaks at 529.7 [46], 530.9 [42], 531.6 and 533.1 eV [47] can be indexed to Fe_3O_4 , and peaks at 529.8, 531.8 eV are indexed to NiFe_2O_4 , respectively [42]. From the peaks indicated in Fig. 1c, in the recorded binding energies spectra Ni $2p_{3/2}$ at 854.9 [48], 856.0 [42] and 861.4 eV [42] along with Ni $2p_{1/2}$ peak at 872.6 eV [44] are respond to NiFe_2O_4 as previously reported [45]. Based on the observation, the chemical states of Ni and Fe in the DAF and DAFN are summarized as Ni^{2+} , Fe^{2+} and Fe^{3+} , respectively. In a word, the XPS results can be consistent with the XRD patterns.

To obtain an intuitive description, digital images were taken to give a better understanding of the product. Observed from Figure S4, the melt-spun alloy ribbon precursors of AF and AFN exhibited a mean size distribution as measured in Table S2

without distinct differences of mechanical strength and ductility before the etching process. Hence, an in-depth research on the microstructure and morphology of the NaOH solution eroded products was probed by high magnification SEM images shown in Fig. 2. From the detailed structure in Fig. 2b, the DAF was evidenced to own an inhomogeneous cluster dispersion with irregular shapes (sheet-like or octahedrons) accompanied with numerous smaller particles and slices attached. Regardless of morphology, the remaining pieces after dealloying with sizes range from 100 nm to over 1 μm . As the state-of-the-art literatures have mentioned about the dealloying procedures, this natural phenomenon is due to the Al removal along with the gradual island aggregation of the partly dissolved Fe component [36, 49]. Meanwhile, these rough aggregates underwent an oxidation under the O containing condition and formed Fe_3O_4 eventually [38]. It is interesting to note that in contrast with DAF sample, most of the DAFN nanosheets in Fig. 2c have at least one straight edge or a corner of around 120° . The magnified image in the inset directly witnessed the smooth arrayed regular hexagon morphology of the nanosheets in the DAFN. The side lengths distribution of each edge is

Figure 2 **a** Brief illustration on the structure evolution of DAFN from alloy precursor to dealloyed product, SEM image showing the microstructure of the two products etched by 2 M NaOH for 48 h in air: **b** DAF sample, (**c** and inset) DAFN sample, respectively.



50–500 nm, thus can be deduced that the scale of the complete breadth ranges from 100 nm to 1 μm , close to but more homogeneous than that of DAF. Besides, the thickness of these sheets in Fig. 2c is so slim that some of the parts are semi-transparent. As described [50], any divalent metal ions with radii close to each other (Ni and Fe have the close atom radii) can constitute the two-dimensional (2D) layered double hydroxides $[\text{Ni}_{1-x}^{2+}\text{Fe}_x^{3+}(\text{OH})_2]^{x+}(\text{A}^{n-})_{x/n}\cdot m\text{H}_2\text{O}$ in theory. Therefore, the morphology of interlaced quasi-hexagonal morphology and the existence of H_2O and NiO at the surface was finally confirmed based on these testimonies, and the morphology evolution is resumed in Fig. 2a. Thus, we can assume that the existence of Ni does affect the formation of morphology in the light of the same external conditions. To further confirm the assumption, EDS elemental mapping was carried out to elaborate their elements distribution. Recognized from the elemental distribution of Fe, O and Al shown in Figure S5, a conclusion was drawn that Ni, Fe and O have a uniform dispersion and all the Al species in the AFN sample was completely removed. In the meantime, Figure S6 reveals the DAF sample possessing homogenous Fe and O dispersion. These results hinted the Fe_3O_4 and NiFe_2O_4 can be co-exist and well interlaced with each other in the sample without adulterate aluminiferous ingredient.

Low-magnification and high-resolution TEM measurements were conducted to confirm the texture and crystalline orientation of the two nanostructures. As

shown in Fig. 3a, a detailed view shows that the DAF structure consists of several irregular slices and nanoparticles with different thicknesses and width, which is similar to its SEM images. Figure 3c displays its corresponding HRTEM images with the interplanar spacings of 0.186, 0.230 and 0.257 nm are align with the (331), (400) and (311) reflection of cubic Fe_3O_4 which is well in accordance with the XRD peaks as pointed in Fig. 1a. More than the existence of Fe_3O_4 in DAF sample, high-resolution TEM image in Fig. 3d points out the DAFN sample has the lattice spacing 0.187 and 0.214 nm could well be indexed to the (311) and (400) in-plane structural parameter of the cubic NiFe_2O_4 . Moreover, in view of Fig. 3b, there is a broken quasi-hexagonal nanosheet in the DAFN sample as the dash line marked out. The TEM and HRTEM results further approved our assumption that Ni doping is in favor of forming hexagonal sheets and uniform distributing of Fe_3O_4 and NiFe_2O_4 during the DAFN products dealloying process.

The Li-ion storage ability of the DAF and DAFN for anode materials were testified by various electrochemical tests. The initial 3 cycles of the charge/discharge profiles of the DAF product (Fig. 4a) and DAFN product (Fig. 4b) composites were obtained at a current rate of 200 mA g^{-1} within a voltage window ranges from 0.01 to 3.0 V. From the first discharge and charge curves in Fig. 4b, a discharge flat stage at around 0.7 V and a charge extended slope from 1.0 to 2.0 V can be observed for the DAFN composite, similar to the literature results for

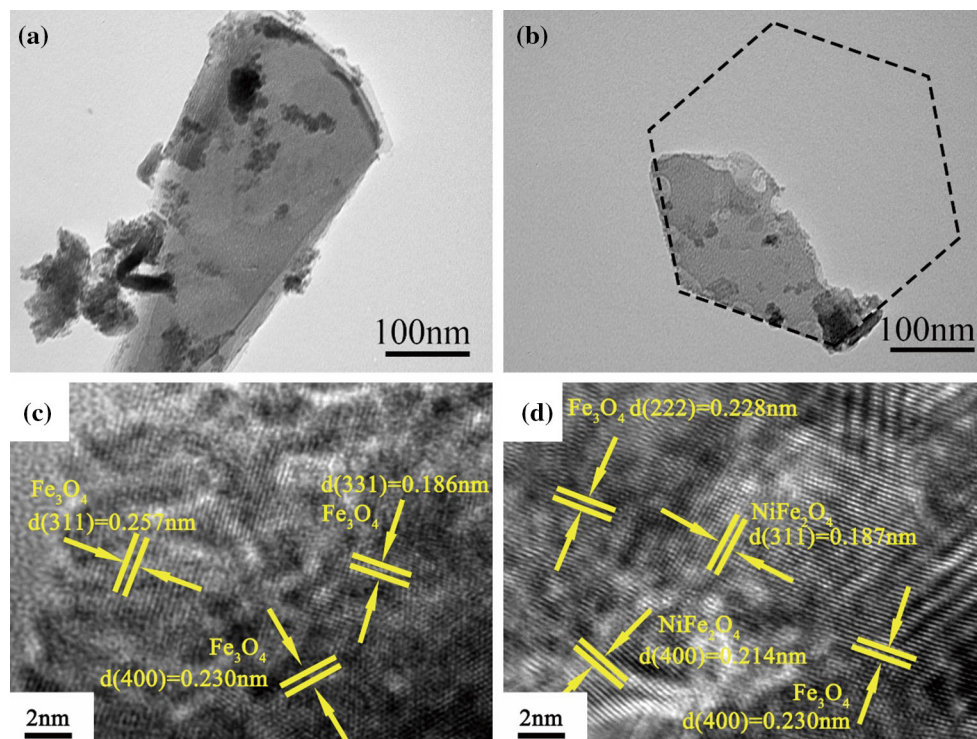
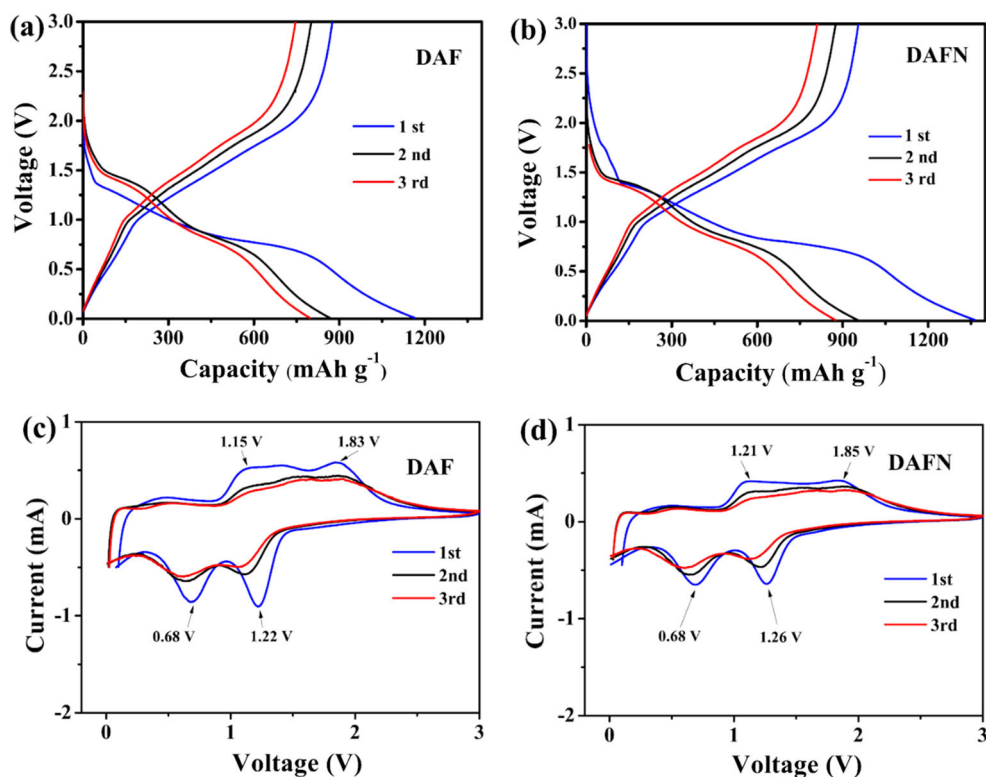
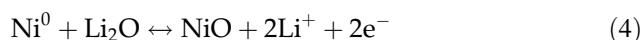
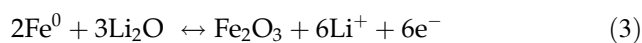
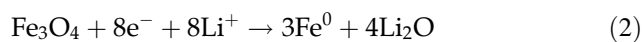


Figure 3 TEM images of DAF sample (a), DAFN sample (b) and HRTEM images of DAF sample (c), DAFN sample (d) from the fresh dealloyed products by 2 M NaOH etching for 48 h in air.

Figure 4 Galvanostatic charge/discharge profiles: a DAF and b DAFN at the current of 200 mA g^{-1} and voltage range from 0.01 to 3 V versus Li. Cyclic voltammetry (CV) curves of c DAF and d DAFN anodes at a scan rate of 0.1 mV s^{-1} from 0.01 to 3 V.



NiFe₂O₄ [51] and Fe₃O₄ [28, 52]. Compared with the DAF, the charge/discharge profiles are the same but for a bit higher than it, which is attributed to the higher potential of Ni-containing [51]. During the processes, the main electrochemical reaction formulas are summarized as:



According to formulas (1) and (2), if 8 mol Li⁺ were embedded, 912 and 926 mAh g⁻¹ discharge capacities would be obtained in 1 mol of NiFe₂O₄ or Fe₃O₄ [53], respectively. It is interesting to note that both DAF and DAFN discharge capacities in the first cycle are 1163.9 and 1364.7 mAh g⁻¹, which evidently exceeded their theoretical capacity by uptaking dozen mols of Li. The formation of solid electrolyte interface (SEI) layers on the electrode surface [54] and amorphous Li₂O [55] before stabilizing, the decomposition of the electrolyte [56] in the first cycle, combining with formulas (3) and (4), could rationally explain the exceeded lithium storage in the initial cycling and the capacity fading phenomenon in the following cycles as well [57].

Figure 4c and d convey the initial cyclic voltammetry curves of the DAF and DAFN electrode over the voltage range of 0.01–3.0 V at a scanning rate of 0.1 mV s⁻¹, respectively. In the first DAFN cathodic process, the broad peaks at 0.68 and 1.26 V are attributed to the reduction of NiFe₂O₄ and Fe₃O₄ to metallic Ni and Fe, along with the irreversible formation of SEI and Li₂O. During the anode scan, two broad oxidation peaks at 1.21 and 1.85 V are ascribed to the oxidation of Fe and Ni to Fe³⁺ and Ni²⁺, and the decomposition of the SEI and Li₂O, respectively, which is in well accordance with the charge/discharge profiles. As shown in Fig. 4c, the DAF sample has the similar but lower cathode peaks at 0.68 and 1.22 V associated with anode peaks at 1.15 and 1.83 V [54, 55]. In the following cycles, compared with the first cycle, two anode and cathode peaks of DAF and DAFN slightly shift due to the electrochemical reaction generated Fe₂O₃ instead of Fe₃O₄ and then caused the potential change [26]. This phenomenon can also illustrate the irreversible electrochemical reactions and capacity fading in the initial several

cycles, which is well consistent with the charge/discharge profiles and formulas (3) and (4).

The cycling performance and the capacity retention of the DAF and DAFN anode material were conducted at the current density of 200 mA g⁻¹. It can be seen from Fig. 5a that the DAFN sample owns a higher capacity (~ 1437 mAh g⁻¹) than that of DAF (~ 1164 mAh g⁻¹) in the first cycling, which can be attributed to the residual Ni²⁺ in the ferrite can provide capacity effectively, but the remaining Fe²⁺ cannot due to its instability and a tendency to be in situ oxidized to Fe³⁺ in the reaction system. As is confirmed in the charge/discharge profiles, the practical capacities far beyond their theoretical capacities in the first discharge of the two compounds, which is commonly happened in lithium battery anode materials due to massive irreversible reactions happened in the first cycle. In other words, multitudinous defects such as vacancies, distortions and dislocations in their nanostructures are able to provide active sites for efficient intercalation of lithium ions. Upon cycling, even though the capacity quickly faded in the initial 150 cycles, the DAFN composite upturned steadily from the 150th cycle, earlier and stronger than DAF sample. This performance made the DAFN product quickly recovered to the doubled capacity afterward, held the doubled reversible capacity over 500 mAh g⁻¹ than the DAF sample after 750 cycles. This appearance could be well documented as the gradually settled complicated processes, the self-reconstructed structure of the electrode materials [58–60], and the reversible growth of a polymeric gel-like film resulting from kinetically activated electrolyte degradation in the literature [61, 62]. Particularly, from 500 to 700 cycles, the cycled DAFN composite held a higher Coulombic efficiency reached to more than 99% with a nearly double reversible discharge capacity than the DAF. The above results indicate the enhanced cycling stability of the DAFN can be ascribed to the interlaced nanosheets enable to hold sufficient space for volume expansion upon conversion reactions, limiting the detachment of active materials effectively and favors fast electron and ion transport during cycling.

The rate capability of the tested samples was cycled at a current density of 100 mA g⁻¹ for the first 30 cycles and then increased the rate from 200 to 2000 mA g⁻¹ step by step. As shown in Fig. 5b, the DAFN composite pronounces a much better performance at lower current density (≤ 500 mA g⁻¹) with

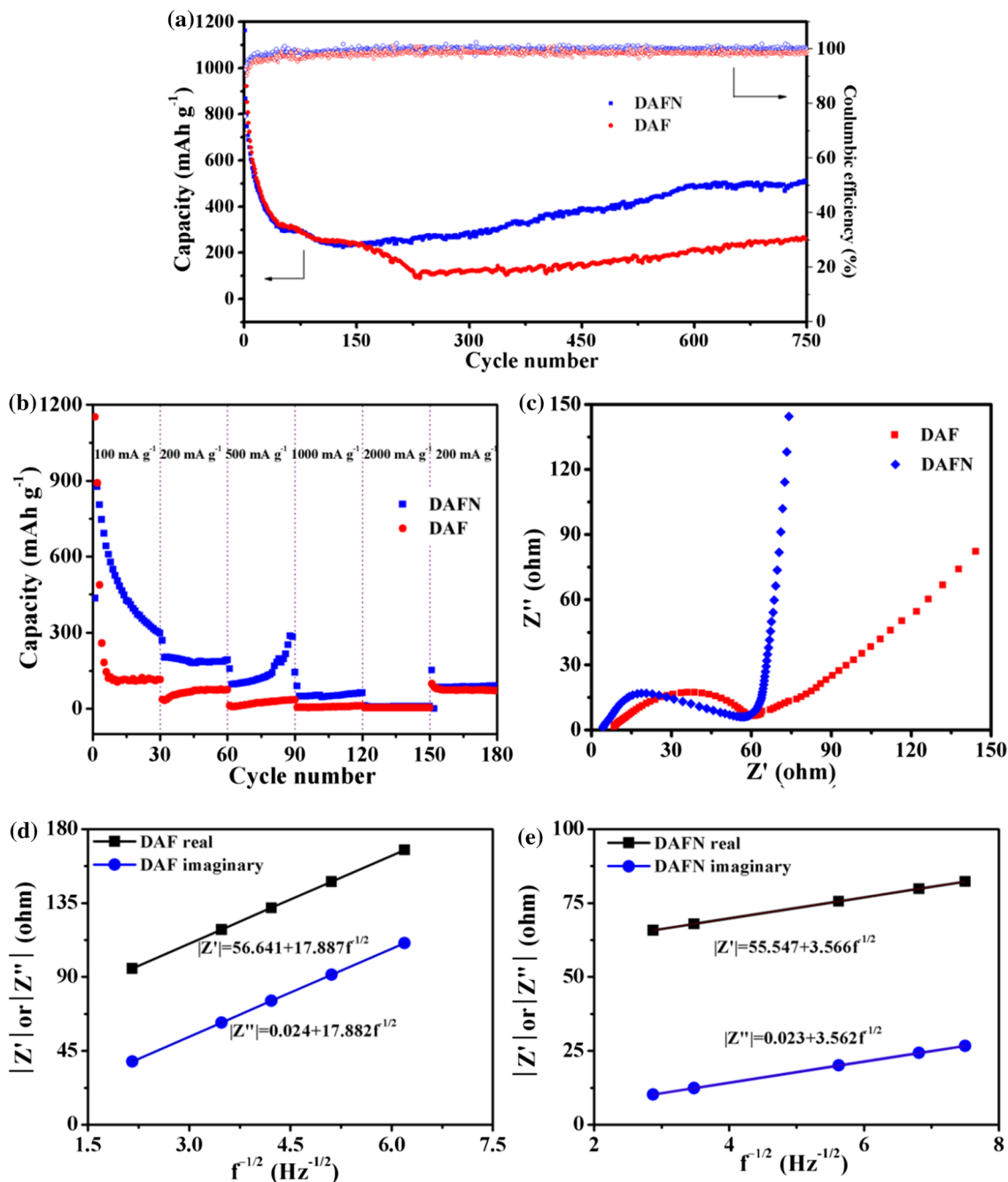


Figure 5 **a** Cyclic performance of DAF and DAFN product and Coulombic efficiency of DAFN in the voltage between 0.01 and 3.0 V 200 mA g⁻¹, **b** Rate performance of the DAF and DAFN at the current density ranges from 100 to 2000 mA g⁻¹,

c Electrochemical impedance spectra of the DAF and DAFN samples, the plotting resistance and imaginary resistance versus inverse square root of the angular frequency of the samples: **d** DAF, **e** DAFN.

double the restored capacities of the DAF composite. These results clearly show that the morphology with interlaced nanosheets plays an important role in improving the electrochemical performance. The improved reversible stable capacity and rate performance can retrospect to the interlaced two-

dimensional nanostructure which is able to accelerate Li-ion transport, alleviate the internal stress, and avoid pulverization of the active material. In the meantime, the synergistic effect [26] of the furnished Fe₃O₄/NiFe₂O₄ interconnected nanosheets could establish fast channels for electron transfer upon

Table 1 The fitted electrochemical impedance parameters calculation of the two samples

Sample	R_e (Ω)	$R_e + R_{ct}$ (Ω)	R_{ct} (Ω)	A_r	A_i	σ
DAF	8.446	59.339	50.893	17.887	17.882	17.884
DAFN	4.048	56.872	52.824	3.566	3.562	3.564

cycling, which is further improved by EIS measurements.

To understand the superior electrochemical performance of the fast ion diffusion and electron transfer of the DAFN sample, electrochemical impedance spectra (EIS) and Warburg factor calculation were carried out after battery activation. From Fig. 5c, we could see that each Nyquist plot consists of an intercept in the high frequency at the Z_{real} axis, a semicircle in the middle frequency and an inclined line in the low frequency region, which could correspond to the electrolyte resistance (R_e), the charge transfer resistance (R_{ct}) and the Warburg factor (σ), respectively. By comparison, it is clear that the DAFN sample has a shorter intercept, indicating the lower R_e than the DAF sample. For a quantitative analysis of the parameters, the impedance spectra were fitted by ZSIMPWIN software, the simulating plots with fitting circuits are shown in Figure S7 and calculation results are listed in Table 1. Results illustrate that DAFN has a lower $R_e + R_{ct}$ of 59.339 Ω than DAF of 56.872 Ω , which could well explain that DAFN owns an enhanced electronic conductivity. In a word, the doping of Ni is in favor of electron transfer.

Based on the EIS measurements, the product information of lithium ion diffusion can be represented by Warburg factors (σ), its formula is shown as follows:

$$\sigma = \frac{A_r + A_i}{2} \quad (5)$$

$$|Z'| = A_r(2\pi f)^{-1/2} \quad (6)$$

$$|Z''| = A_i(2\pi f)^{-1/2} \quad (7)$$

where f is the frequency, $|Z'|$ and $|Z''|$ are the real and imaginary resistance, and the corresponding Warburg factor (σ) could be obtained by figuring out the mean value of A_r and A_i , the two parameters which means the slope of $|Z'|$ versus $f^{-1/2}$ and $|Z''|$ versus $f^{-1/2}$, respectively [63]. In view of the lower Warburg factor in Fig. 5d and e, it is favorable to demonstrate that the DAFN sample has the faster ion diffusion. In general, with the help of the synergistic effect of $\text{Fe}_3\text{O}_4/\text{NiFe}_2\text{O}_4$, the DAFN sample performs well in

both electron transfer and ion diffusion and thus can lead to a lower resistance and an enhanced rate performance before cycling.

Conclusion

In summary, we successfully fabricated two-dimensional nanosheets with homogenous distribution of $\text{Fe}_3\text{O}_4/\text{NiFe}_2\text{O}_4$ by a facile chemical dealloying of the AFN sample. The as-prepared interlaced nanosheets and interconnected voids exhibited excellent volume change tolerance, fast ion and electron transportation. The DAFN also expressed doubled cycling capacities over 500 mAh g^{-1} after long-term cycles and modified rate performances than DAF products at a low cost. The well-behaved product and concise synthesis illuminate a promising prospect as a novel anode material manufacturing for next-generation high-performance LIBs.

Acknowledgements

We gratefully acknowledge the support of this research by the Science and Technology Research Project of the Education Department of Jilin Province during the 13th five-year-plan period (No. 2016-359), the Natural Science Foundation of Jilin Province (No. 20170101128JC), Industrial Technology Research and Development Project of Jilin Province Development and Reform Commission (No. 2017C052-4) and National Natural Science Foundation of China (No. 201601018).

Compliance with ethical standards

Conflict of interest The authors declare there is no conflict of interest.

Electronic supplementary material: The online version of this article (<https://doi.org/10.1007/s10853-018-2729-y>) contains supplementary material, which is available to authorized users.

References

- [1] Goodenough JB, Park KS (2013) The Li-ion rechargeable battery: a perspective. *J Am Chem Soc* 135:1167–1176. <https://doi.org/10.1021/ja3091438>
- [2] Tarascon JM, Armand M (2001) Issues and challenges facing rechargeable lithium batteries. *Nature* 414:359–367. <https://doi.org/10.1038/35104644>
- [3] Kang B, Ceder B (2009) Battery materials for ultrafast charging and discharging. *Nature* 458:190–193. <https://doi.org/10.1038/nature07853>
- [4] Ji LW, Lin Z, Alcoutlabi M, Zhang XW (2011) Recent developments in nanostructured anode materials for rechargeable lithium-ion batteries. *Energy Environ Sci* 4:2682–2699. <https://doi.org/10.1039/c0ee00699h>
- [5] Balogun MS, Qiu WT, Luo Y, Meng H, Mai WJ, Onasanya A, Olaniyi TK, Tong YX (2016) A review of the development of full cell lithium-ion batteries: the impact of nanostructured anode materials. *Nano Res* 9:2823–2851. <https://doi.org/10.1007/s12274-016-1171-1>
- [6] Poizot P, Laruelle S, Grugeon S, Dupont L, Tarascon JM (2000) Nano-sized transition-metal oxides as negative-electrode materials for lithium-ion batteries. *Nature* 407:496–499. <https://doi.org/10.1038/35035045>
- [7] Wu HB, Chen JS, Hng HH, Lou XW (2012) Nanostructured metal oxide-based materials as advanced anodes for lithium ion batteries. *Nanoscale* 4:2526–2542. <https://doi.org/10.1039/c2nr11966h>
- [8] Courtel FM, Duncan H, Abu-Lebdeh Y, Davidson IJ (2011) High capacity anode materials for Li-ion batteries based on spinel metal oxides AMn_2O_4 ($A = Co, Ni$ and Zn). *J Mater Chem* 21:10206–10218. <https://doi.org/10.1039/c0jm04465b>
- [9] Liu H, Wang XL, Xu H et al (2017) Nanostructured CoO/NiO/CoNi with tunable morphology for high performance lithium-ion batteries. *Dalton Trans* 46:11031–11036. <https://doi.org/10.1039/c7dt01904a>
- [10] Balogun MS, Qiu WT, Luo Y et al (2015) Improving the lithium-storage properties of self-grown nickel oxide: a back-up from TiO_2 nanoparticles. *ChemElectroChem* 2:1243–1248. <https://doi.org/10.1002/celec.201500146>
- [11] Huang XH, Tu JP, Zhang B, Li Y, Yuan YF, Wu HM (2006) Electrochemical properties of NiO–Ni nanocomposite as anode material for lithium ion batteries. *J Power Sources* 161:541–544. <https://doi.org/10.1016/j.jpowsour.2006.03.039>
- [12] Luo Y, Balogun MS, Qiu WT, Zhao RR, Liu P, Tong YX (2015) Sulfurization of FeOOH nanorods on a carbon cloth and their conversion into Fe_2O_3/Fe_3O_4 -S core-shell nanorods for lithium storage. *Chem Commun* 51:13016–13019. <https://doi.org/10.1039/c5cc04700e>
- [13] Hua MQ, Xu L, Cui L et al (2018) Hexamethylenetetramine-assisted hydrothermal synthesis of octahedral nickel ferrite oxide nanocrystallines with excellent supercapacitive performance. *J Mater Sci* 53:7621–7636. <https://doi.org/10.1007/s10853-018-2052-7>
- [14] Thankachan RM, Rahman MM, Sultana I, Glushenkov AM, Thomas S, Kalarikkal N, Chen Y (2015) Enhanced lithium storage in $ZnFe_2O_4$ -C nanocomposite produced by a low-energy ball milling. *J Power Sources* 282:462–470. <https://doi.org/10.1016/j.jpowsour.2015.02.039>
- [15] Zhang H, Zhao YM, Wen MM, Dong YZ, Fan QH, Kuang Q, Liu HT, Lian X (2018) A new sodium ferrous orthophosphate $Na_xFe_4(PO_4)_3$ as anode materials for sodium-ion batteries. *J Mater Sci* 53:8385–8397. <https://doi.org/10.1007/s10853-018-2128-4>
- [16] Nie LY, Wang HJ, Ma JJ, Liu S, Yuan R (2016) Sulfur-doped $ZnFe_2O_4$ nanoparticles with enhanced lithium storage capabilities. *J Mater Sci* 52:3566–3575. <https://doi.org/10.1007/s10853-016-0373-y>
- [17] Zhai XM, Xu XM, Zhu XL, Zhao YJ, Li JB, Jin HB (2018) Porous layer assembled hierarchical Co_3O_4 as anode materials for lithium-ion batteries. *J Mater Sci* 53:1356–1364. <https://doi.org/10.1007/s10853-017-1579-3>
- [18] Takahisa S, Shigeto O, Shin-ichi T, Yun-ichi Y (1996) Study of $Li_{3-x}M_xN$ ($M: Co, Ni$ or Cu) system for use as anode material in lithium rechargeable cells. *Solid State Ion* 86–88:785–789. [https://doi.org/10.1016/0167-2738\(96\)00174-9](https://doi.org/10.1016/0167-2738(96)00174-9)
- [19] Liu DS, Liu DH, Hou BH, Wang YY, Guo JZ, Ning QL, Wu XL (2018) 1D porous MnO@N-doped carbon nanotubes with improved Li-storage properties as advanced anode material for lithium-ion batteries. *Electrochim Acta* 264:292–300. <https://doi.org/10.1016/j.electacta.2018.01.129>
- [20] Ji XY, Li D, Lu QF, Guo EY, Yao LB, Liu H (2018) Electrospinning preparation of one-dimensional Co^{2+} -doped $Li_4Ti_5O_{12}$ nanofibers for high-performance lithium ion battery. *Ionics*. <https://doi.org/10.1007/s11581-018-2453-2>
- [21] Hao SJ, Zhang BW, Wang Y et al (2018) Hierarchical three-dimensional Fe_3O_4 @porous carbon matrix/graphene anodes for high performance lithium ion batteries. *Electrochim Acta* 260:965–973. <https://doi.org/10.1016/j.electacta.2017.12.078>
- [22] Wang JX, Xiong Y, Zhang XH (2016) Rational synthesis of $NiCo_2O_4$ meso-structures for high-rate supercapacitors. *J Mater Sci* 52:3678–3686. <https://doi.org/10.1007/s10853-016-0658-1>
- [23] Li J, Xu SJ, Huang S, Lu L, Lan LF, Li SF (2017) In situ synthesis of $Fe_{(1-x)}Co_xF_3$ /MWCNT nanocomposites with excellent electrochemical performance for lithium-ion

- batteries. *J Mater Sci* 53:2697–2708. <https://doi.org/10.1007/s10853-017-1685-2>
- [24] Poizot P, Laruelle S, Grubeon S, Dupont L, Tarascon JM (2001) Searching for new anode materials for the Li-ion technology: time to deviate from the usual path. *J Power Sources* 97–98:235–239. [https://doi.org/10.1016/S0378-7753\(01\)00508-0](https://doi.org/10.1016/S0378-7753(01)00508-0)
- [25] Shin WH, Jeong HM, Kim BG, Kang JK, Choi JW (2012) Nitrogen-doped multiwall carbon nanotubes for lithium storage with extremely high capacity. *Nano Lett* 12:2283–2288. <https://doi.org/10.1021/nl3000908>
- [26] Feng XS, Huang Y, Chen XF, Wei C, Zhang X, Chen MH (2017) Hierarchical CoFe₂O₄/NiFe₂O₄ nanocomposites with enhanced electrochemical capacitive properties. *J Mater Sci* 53:2648–2657. <https://doi.org/10.1007/s10853-017-1735-9>
- [27] Walle MD, Zhang ZF, Zhang MY, You XL, Li YJ, Liu YN (2017) Hierarchical 3D nitrogen and phosphorous codoped graphene/carbon nanotubes–sulfur composite with synergistic effect for high performance of lithium–sulfur batteries. *J Mater Sci* 53:2685–2696. <https://doi.org/10.1007/s10853-017-1678-1>
- [28] Qiu WT, Balogun MS, Luo Y et al (2016) Three-dimensional Fe₃O₄ nanotube array on carbon cloth prepared from a facile route for lithium ion batteries. *Electrochim Acta* 193:32–38. <https://doi.org/10.1016/j.electacta.2016.01.173>
- [29] Yuan CZ, Wu HB, Xie Y, Lou XW (2014) Mixed transition-metal oxides: design, synthesis, and energy-related applications. *Angew Chem Int Ed* 53:1488–1504. <https://doi.org/10.1002/anie.201303971>
- [30] Li XF, Dhanabalan A, Wang CL (2011) Enhanced electrochemical performance of porous NiO–Ni nanocomposite anode for lithium ion batteries. *J Power Sources* 196:9625–9630. <https://doi.org/10.1016/j.jpowsour.2011.06.097>
- [31] Wu SH, Fu GL, Lv WQ et al (2018) A single-step hydrothermal route to 3D hierarchical Cu₂O/CuO/rGO nanosheets as high-performance anode of lithium-ion batteries. *Small* 14:1702667. <https://doi.org/10.1002/smll.201702667>
- [32] Su DW, Kim HS, Kim WS, Wang GX (2012) Mesoporous nickel oxide nanowires: hydrothermal synthesis, characterization and applications for lithium-ion batteries and supercapacitors with superior performance. *Chem Eur J* 18:8224–8229. <https://doi.org/10.1002/chem.201200086>
- [33] Qin J, Liu DY, Zhao NQ et al (2018) Fabrication of Sn-core/CNT-shell nanocable anchored interconnected carbon networks as anode material for lithium ion batteries. *Mater Lett* 212:94–97. <https://doi.org/10.1016/j.matlet.2017.10.011>
- [34] Han JZ, Qin J, Guo LC et al (2018) Ultrasmall Fe₂GeO₄ nanodots anchored on interconnected carbon nanosheets as high-performance anode materials for lithium and sodium ion batteries. *Appl Surf Sci* 427:670–679. <https://doi.org/10.1016/j.apsusc.2017.08.026>
- [35] Helle S, Pedron M, Assouli B, Davis B, Guay D, Roué L (2010) Structure and high-temperature oxidation behaviour of Cu–Ni–Fe alloys prepared by high-energy ball milling for application as inert anodes in aluminium electrolysis. *Corros Sci* 52:3348–3355. <https://doi.org/10.1016/j.corsci.2010.06.011>
- [36] Xu CX, Wang RY, Zhang Y, Ding Y (2010) A general corrosion route to nanostructured metal oxides. *Nanoscale* 2:906–909. <https://doi.org/10.1039/b9nr00351g>
- [37] Liu H, Wang XL, Wang JX, Xu H, Yu WS, Dong XT, Zhang HB, Wang LM (2017) Hierarchical porous CoNi/CoO/NiO composites derived from dealloyed quasicrystals as advanced anodes for lithium-ion batteries. *Scripta Mater* 139:30–33. <https://doi.org/10.1016/j.scriptamat.2017.06.011>
- [38] Liu H, Wang XL, Wang JX, Xu H, Yu WS, Dong XT, Zhang HB, Wang LM (2017) High electrochemical performance of nanoporous Fe₃O₄/CuO/Cu composites synthesized by dealloying Al–Cu–Fe quasicrystal. *J Alloys Compd* 729:360–369. <https://doi.org/10.1016/j.jallcom.2017.09.111>
- [39] Zhang J, Ling YH, Gao WB, Wang S, Li JT (2013) Enhanced photoelectrochemical water splitting on novel nanoflake WO₃ electrodes by dealloying of amorphous Fe–W alloys. *J Mater Chem A* 1:10677–10685. <https://doi.org/10.1039/c3ta12273e>
- [40] Huber GW, Shabaker JW, Dumesic JA (2003) Raney Ni–Sn catalyst for H₂ production from biomass-derived hydrocarbons. *Science* 300:2075–2077. <https://doi.org/10.1126/science.1085597>
- [41] Kittler S, Greulich C, Diendorf J, Köller M, Epple M (2010) Toxicity of silver nanoparticles increases during storage because of slow dissolution under release of silver ions. *Chem Mater* 22:4548–4554. <https://doi.org/10.1021/cm100023p>
- [42] Biesinger MC, Payne BP, Grosvenor AP, Lau LWM, Gerson AR, Smart RSC (2011) Resolving surface chemical states in XPS analysis of first row transition metals, oxides and hydroxides: Cr, Mn, Fe, Co and Ni. *Appl Surf Sci* 257:2717–2730. <https://doi.org/10.1016/j.apsusc.2010.10.051>
- [43] Anderson JF, Kuhn M, Diebold U (1996) Epitaxially grown Fe₃O₄ thin films: an XPS study. *Surf Sci Spectra* 4:266–272. <https://doi.org/10.1116/1.1247796>
- [44] Liu PB, Huang Y, Zhang X (2014) Enhanced electromagnetic absorption properties of reduced graphene oxide–polypyrrole with NiFe₂O₄ particles prepared with simple hydrothermal method. *Mater Lett* 120:123–146. <https://doi.org/10.1016/j.matlet.2014.01.054>

- [45] Chen LY, Dai H, Shen YM, Bai JF (2010) Size-controlled synthesis and magnetic properties of NiFe_2O_4 hollow nanospheres via a gel-assistant hydrothermal route. *J Alloys Compd* 491:L33–L38. <https://doi.org/10.1016/j.jallcom.2009.11.031>
- [46] Cheng FY, Su CH, Yang YS, Yeh CS, Tsai CY, Wu CL, Wu MT, Shieh DB (2005) Characterization of aqueous dispersions of Fe_3O_4 nanoparticles and their biomedical applications. *Biomaterials* 26:729–738. <https://doi.org/10.1016/j.biomaterials.2001.03.016>
- [47] Langell MA, Wilson D (2014) XPS analysis of oleylamine/oleic acid capped Fe_3O_4 nanoparticles as a function of temperature. *Appl Surf Sci* 303:6–13. <https://doi.org/10.1016/j.apsusc.2014.02.006>
- [48] Ren A, Liu CB, Hong YZ, Shi WD, Lin S, Li P (2014) Enhanced visible-light-driven photocatalytic activity for antibiotic degradation using magnetic $\text{NiFe}_2\text{O}_4/\text{Bi}_2\text{O}_3$ heterostructures. *Chem Eng J* 258:301–308. <https://doi.org/10.1016/j.cej.2014.07.071>
- [49] Hao Q, Li MH, Jia SZ, Zhao XY, Xu CX (2013) Controllable preparation of Co_3O_4 nanosheets and their electrochemical performance for Li-ion batteries. *RSC Adv* 3:7850–7854. <https://doi.org/10.1039/c3ra23448g>
- [50] Long X, Wang ZL, Xiao S, An YM, Yang SH (2016) Transition metal based layered double hydroxides tailored for energy conversion and storage. *Mater Today* 19:213–226. <https://doi.org/10.1016/j.mattod.2015.10.006>
- [51] Cherian CT, Sundaramurthy J, Reddy MV et al (2013) Morphologically robust NiFe_2O_4 nanofibers as high capacity Li-ion battery anode material. *ACS Appl Mater Interfaces* 5:9957–9963. <https://doi.org/10.1021/am401779p>
- [52] Zhou GM, Wang DW, Li F et al (2010) Graphene-wrapped Fe_3O_4 anode material with improved reversible capacity and cyclic stability for lithium ion batteries. *Chem Mater* 22:5306–5313. <https://doi.org/10.1021/cm101532x>
- [53] Zhao XY, Xia DG, Zheng K (2012) $\text{Fe}_3\text{O}_4/\text{Fe}/\text{Carbon}$ composite and its application as anode material for lithium-ion batteries. *ACS Appl Mater Interfaces* 4:1350–1356. <https://doi.org/10.1021/am201617j>
- [54] Li H, Huang XJ, Chen LQ (1999) Direct imaging of the passivating film and microstructure of nanometer-scale SnO anodes in lithium rechargeable batteries. *Electrochem Solid-State Lett* 1:241–243. <https://doi.org/10.1149/1.1390699>
- [55] Li H, Shi LH, Lu W, Huang XJ, Chen LQ (2001) Studies on capacity loss and capacity fading of nanosized SnSb alloy anode for Li-ion batteries. *J Electrochem Soc* 148:A915–A922. <https://doi.org/10.1149/1.1383070>
- [56] Stjern Dahl M, Bryngelsson H, Gustafsson T, Vaughey JT, Thackeray MM, Edström K (2007) Surface chemistry of intermetallic AlSb -anodes for Li-ion batteries. *Electrochim Acta* 52:4947–4955. <https://doi.org/10.1016/j.electacta.2007.01.064>
- [57] Zhang H (2011) A review of the electrochemical performance of alloy anodes for lithium-ion batteries. *J Power Sources* 196:13–24. <https://doi.org/10.1016/j.jpowsour.2010.07.020>
- [58] Laruelle S, Grugeon S, Poizot P, Dollé M, Dupont L, Tarascon JM (2002) On the origin of the extra electrochemical capacity displayed by MO/Li cells at low potential. *J Electrochem Soc* 149:A627–A634. <https://doi.org/10.1149/1.1467947>
- [59] Do JS, Weng CH (2005) Preparation and characterization of CoO used as anodic material of lithium battery. *J Power Sources* 146:482–486. <https://doi.org/10.1016/j.jpowsour.2005.03.095>
- [60] Wang Y, Huang ZG, Wang YY (2015) A new approach to synthesize $\text{MoO}_2@\text{C}$ for high-rate lithium ion batteries. *J Mater Chem A* 3:21314–21320. <https://doi.org/10.1039/c5ta05345e>
- [61] Kang WP, Tang YB, Li WY, Yang X, Xue HT, Yang QD, Lee CS (2015) High interfacial storage capability of porous $\text{NiMn}_2\text{O}_4/\text{C}$ hierarchical tremella-like nanostructures as lithium ion battery anode. *Nanoscale* 7:225–231. <https://doi.org/10.1039/c4nr04031g>
- [62] Zhang LH, Zhu SQ, Cao H, Hou LR, Yuan CZ (2015) Hierarchical porous ZnMn_2O_4 hollow nanotubes with enhanced lithium storage toward lithium-ion batteries. *Chem Eur J* 21:10771–10777. <https://doi.org/10.1002/chem.201501421>
- [63] Xi LJ, Wang HE, Lu ZG, Yang SL, Ma RG, Deng JQ, Chung CY (2012) Facile synthesis of porous LiMn_2O_4 spheres as positive electrode for high-power lithium ion batteries. *J Power Sources* 198:251–257. <https://doi.org/10.1016/j.jpowsour.2011.09.100>